J Mater Sci (2006) 41:5169–5184
DOI 10.1007/s10853-006-0428-6

Texture in solid-state reactions

Jeffrey K. Farrer · C. Barry Carter

Received: 14 July 2005 / Accepted: 27 March 2006 / Published online: 29 July 2006

Abstract The crystallography and texture of solid-state reactions have been studied using electron backscatter diffraction (EBSD) in a scanning electron microscope (SEM). The crystallography of both the reaction interfaces and the grain boundaries plays an important role in the kinetics of the formation of the reaction products. The growth of the reaction products is dependent upon the transport of ions through the material, which is, in turn, affected by both the orientation of the reactants and by grain boundaries in the reactants and in the reaction products. In order to predict or control the behavior of the reactions, the crystallography of all the interfaces present in the reaction must be more fully understood. In the present study, $MgIn_2O_4$ was formed by the reaction between a single-crystal MgO substrate and a thin film of In_2O_3 with and without an applied electric field.

Introduction

For many technologically important oxides, solid-state reactions are either a vital step in the processing of the materials or a result of the environment in which the materials function [1, 2]. In cases where the reaction is part of the processing, the desired material is typically a product of the reaction between two or more other materials. In cases where the reaction is caused by external factors, the result may be a detrimental change in their mechanical and/or electrical properties. The effects of high electric fields on oxides that may be used for their insulating property have been studied previously [3–9]. These studies have shown that where the composite material is subjected to high electric fields, the ionic transport is significantly increased, thus leading to a higher rate of interfacial reactions. This change is particularly important along interfaces where the rate of matter transport is much higher than that through the bulk [10].

The internal factors that influence the rate of solid-state reactions—the kinetic processes which occur in the materials during reactions—can be either interface-controlled or diffusion-controlled. Either case involves the transport of structural elements of the crystal and possibly local reactions between the structural elements. The crystallography of a material and especially crystal imperfections have a significant influence on the transport of structural elements and other kinetic processes that affect the rate of the reaction [11]. Understanding the influence of the crystallography and structural imperfections upon the kinetics of the reaction, requires a complete characterization of the crystallography of the materials present, which must then be associated with the localized behavior of the reaction.

The formation of a spinel by the heterogeneous, solid-state reaction between two oxides is a model system for the study of solid-state reactions. The reasons for this are: first, the close-spaced oxygen sublattices of the materials are very similar; second, the

J. K. Farrer
Department of Physics and Astronomy, Brigham Young University, Provo, UT 84602, USA

C. B. Carter (✉)
Department of Chemical Engineering & Materials Science, University of Minnesota, Minneapolis, MN 55455, USA
e-mail: cbcarter@umn.edu

structure of spinel is relatively simple; and finally, the reaction can generally be treated as a binary reaction [12, 13]. The reaction can, in principle, proceed via numerous different mechanisms. In the absence of oxygen transport, via the solid or gas phase, the reaction proceeds by the counterdiffusion of cations [14], or the transport of the cations across the reaction product layer and into the opposite interface (diffusion-controlled). For example, in the case of MgO and Al_2O_3 reacting to form $MgAl_2O_4$, the reaction would take place by the diffusion of Mg cations through the reaction product layer to the $Al_2O_3/MgAl_2O_4$ interface, and the diffusion of Al cations to the MgO/$MgAl_2O_4$ interface. When the reaction layer is thin, the rate of the reaction is not limited by the diffusion of the cations, but by interfacial processes. In this interface-controlled regime, the reaction rate is typically linear with time, but it is also affected by the misorientations of the reactants [15–17]. As the reaction layer thickens the rate is then dependent upon the transport coefficient of the cations and a driving force. This leads to the diffusion-controlled reaction regime and the well-known and experimentally confirmed parabolic relationship between reaction–product layer thickness and reaction time [18, 19].

It has also been shown, that in some cases, the kinetics of the reaction and the reaction rate are dependent on crystal orientation and the presence and nature of grain boundaries. This effect is most clearly seen when a thin-film geometry is used to study the reaction [15, 16, 20–22]. For example, in cases where polycrystalline NiO or CoO films were reacted with single-crystal Al_2O_3, a difference in reaction rate was observed with different substrate orientation [15, 17]. Also the influence of grain boundaries has been shown in the reaction between NiO films and Al_2O_3 substrates. It was found that there are $\Sigma = 3$ incoherent twin boundaries in the NiO [23], and the intersection of the twin boundaries with the Al_2O_3 acts as a nucleation site for the $NiAl_2O_4$ (spinel) [17, 24].

Spinel-forming reactions may be further complicated by external factors such as the presence of an electric field. The effect of an applied electric field on the formation of $MgFe_2O_4$ and $MgIn_2O_4$ has also been investigated previously [8, 9, 25, 26]. Several of these experiments involved preparing one of the reactants as a thin film, the other reactant acting as the substrate for growth. The thin-film approach was used, in part, to try and isolate the affects of grain-boundary diffusion as opposed to bulk diffusion. It was shown that the kinetics of the reaction were enhanced in the presence of an applied field. It was also shown that the reaction product growth near a grain boundary in the film was very different from growth occurring far from the boundary [9, 25].

Many studies of solid-state reactions have used various techniques to determine and analyze the crystallography of the reactants and reaction products [17, 23, 27–35], but very few have used electron backscatter diffraction (EBSD) to identify the phases and also characterize the orientation texture and the misorientations of the interfaces present in such reactions [8, 10]. The EBSD detection system installed on an scanning electron microscope (SEM) may be used either to identify an unknown crystalline phase [36], or to scan the surface of a crystalline material over a specified area and create an orientation image of the scanned area [37–41]. The advantages of using EBSD become apparent when it is realized that the number of data points and the size of the possible acquisition areas far exceed the number capable of being analyzed by other techniques. Furthermore, the actual resolution of EBSD, which is highly dependent upon the probe size of the host SEM, is much finer than that of X-ray microdiffraction (1–10 μm) or other techniques typically used for texture analysis.

In the present paper, EBSD was used to study the solid-state reaction between In_2O_3 and MgO. The MgO–In_2O_3 system was chosen because of the technological importance of both In_2O_3 and $MgIn_2O_4$ as transparent conducting oxides [42, 43]. In this example, a thin-film approach has been used, where the In_2O_3 is grown as a thin film on a MgO substrate. The growth of In_2O_3 thin films has been studied extensively [44–47] and was not the focus of this study. Therefore, discussion of the thin-film growth will be mainly limited to the agreement or disagreement found with several previous studies [44, 47]. Rather, in the present paper, EBSD was used to determine the phases, the crystallography and the grain character of the solid-state reaction between In_2O_3 and MgO. The influence of an electric field on the rate and nature of the reaction layer growth was also demonstrated. Results from high-resolution secondary electron (SE) imaging and from X-ray energy dispersive spectrometry (XEDS) are combined with the EBSD data to obtain complementary chemical and crystallographic information. It is shown that the use of EBSD allows for a unique analysis of the thin-film reaction.

EBSD analysis

Because of the relatively recent development of the use of automated EBSD detection systems for the study of oxides [48, 49] we will give a brief review of

the systems, and the methods of data analysis will be presented here.

The EBSD detection systems work by acquiring diffraction patterns when the electron beam interacts with a highly tilted (~70°) and well-polished sample. A simplified schematic of the EBSD detection system inside the vacuum chamber of a SEM is shown in Fig. 1. The backscattered electrons from a crystalline sample form Kikuchi-like patterns on a phosphor screen, which is placed approximately 25 μm from the sample. The EBSD patterns are imaged with a digital camera and sent to a computer for processing. The patterns are then analyzed using a mathematical transform to locate band edges in the pattern [50]. The band edges of the pattern are directly related to the locations of the crystal lattice planes. The angles between the planes can then be calculated and used to index the patterns [51].

The scanning capabilities of the SEM allow for the beam to be scanned over a specified area of the surface; at each point an EBSD pattern is acquired and indexed. Using an attached XEDS detector, energy counts for pre-selected elements can simultaneously be collected at each point. A data map of the area is thereby generated which contains for each data point: the Euler angles, representing the orientation of the material; the number of X-ray counts for the elements selected; the band locations and pattern quality; and of course, the x–y coordinates of each data point.

With these data, various maps and plots may be constructed to ''image'' the crystallography and phases of the surface of the material as well as various types of misorientations. For example, the orientations of the sample are most easily illustrated using an inverse pole figure (IPF) map. The IPF map is a color representation of the crystallographic directions of the material parallel to a specified direction. Therefore, if the specified direction is the normal to the surface of the sample, then the IPF map shows, by color, the crystallographic direction of the material that is parallel to the surface normal.

The data, however, are used for more than creating orientation images. The orientations are also typically displayed in a pole figure or a texture pole figure. The pole figure simply plots on a stereographic projection, the orientation of a given plane normal (pole) with respect to the sample reference frame.

The ODF pole figure, however, is calculated using the orientation distribution function (ODF), ($f(g)$), which is a probability density function describing the probability of finding a grain with an orientation g within a given angular distance, Δg, of a specified orientation g_o in a polycrystal; or in other words, the ODF is a way to create a smooth curve fit from the discrete orientations [51, 52]. The data of the ODF pole figure are represented as a stereographic projection, which is divided by contour lines, or different colors, into regions that fall within a given range of occurrence of orientation g. This is reported as a multiple of the random occurrence or random spread of orientation g. The ODF pole figure type analyses can be conducted on every data point or using only one data point per grain.

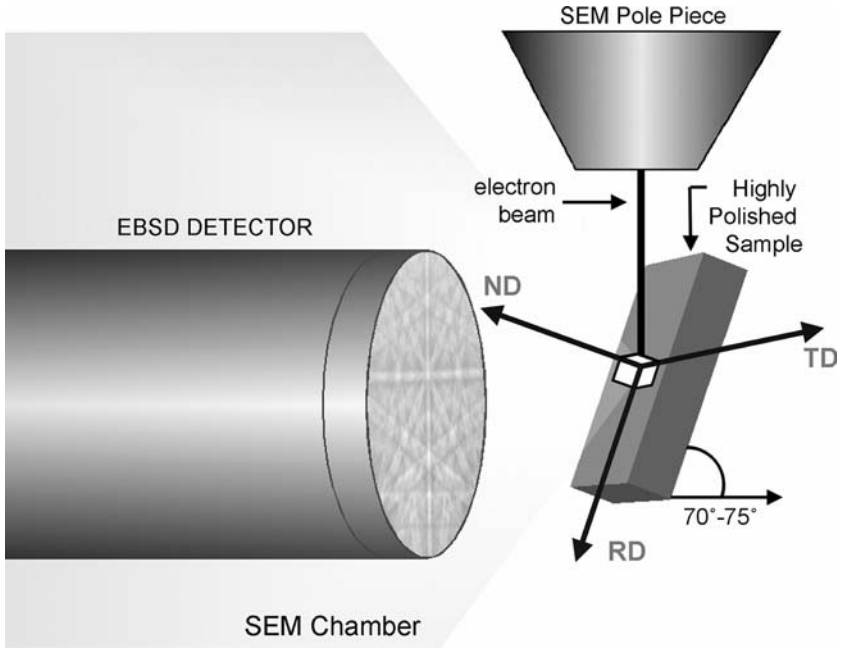

Fig. 1 A simplified schematic of the EBSD automated detection system. The system is attached to the SEM chamber and consists of a phosphor screen placed near a highly tilted (~70°) specimen. The patterns appearing on the phosphor are imaged using a CCD camera and then analyzed by computer. The axes shown on the surface of the sample act as a reference to the orientations acquired by the system. The axis system is labeled ''ND'' (normal direction or 001), ''RD'' (reference direction or 100) and ''TD'' (transverse direction or 010)

Collecting X-ray counts for specific elements allows for more complete phase differentiation. Typically, the crystal structures of different phases are enough to create a distinguishable difference in the EBSD patterns of the respective phases. However, when the structures are similar, the differences in the EBSD patterns may not be enough for the EBSD detection system to differentiate between the phases automatically. In these cases it is necessary to use the X-ray counts to filter the data. For example, if a sample contained two different phases, NiO (cubic, sodium-chloride structure) and $NiAl_2O_4$ (cubic, spinel structure), then it is possible that the automated indexing routine could index an EBSD pattern from one cubic phase or the other with the incorrect material file (it might index a NiO pattern using the $NiAl_2O_4$ material file). In this case, it would be necessary to first ''presort'' the data based on the X-ray energy counts; then constrain the indexing of each pattern to only the material file of the phase that matches the energy counts associated with that pattern [53].

The quality of the EBSD patterns is also collected and can be used to create an image quality (IQ) map. The IQ map is created by measuring the quality (i.e., the degree of contrast of the band edges) of the patterns and assigning a grayscale value—white representing the highest relative pattern quality and black the lowest. The IQ map is useful for locating grain boundaries and other areas of low pattern quality. The grain boundaries typically have a low pattern quality because as the beam crosses the boundary the pattern becomes very weak, or there are two weak overlapping patterns from either side of the boundary. In either case, the pattern quality is relatively lower, and therefore, the boundary appears as a dark line in the IQ map.

In order to identify an unknown crystalline phase, the electron beam is positioned over the material in question, and the chemical composition is acquired using XEDS. The chemistry is then used to search a database of materials files to generate a list of candidate phases. The materials files contain all of the structural information about the material necessary to properly simulate an EBSD pattern. The materials files are then used to attempt to index the EBSD pattern acquired from the same point as the XEDS spectra. The crystallography of the phase is, therefore, identified by correctly indexing the pattern using the crystallographic information of the correct candidate phase from the list [36].

It should be noted that when the EBSD patterns are collected to create the various orientation images or IQ maps the samples are tilted 70° about the *x*-axis (horizontal in the image). Therefore, the incremental step size, at which the patterns are collected, is appropriately shortened in the *y* direction so that the desired step size is maintained with respect to the surface of the sample. Then when the maps are displayed, the data points are shown as if the sample was not tilted. The maps are, therefore, a tilt-corrected image of the surface.

Experimental details

In_2O_3 was deposited by pulsed-laser deposition (PLD) onto cleaved MgO (001) substrates (sodium-chloride structure). Prior to growth, the MgO substrates were cleaved to approximately 1 mm thickness and 10 mm^2. To reference the original interface, a 2 nm layer of Pt was ion-sputtered on the surface of the MgO. The substrates were then heated to 1175 °C at which point the Pt film dewet the surface to create Pt particles smaller than 100 nm. Following the heat treatment the substrates were mounted in the PLD chamber. The KrF (λ = 248 nm) excimer laser of the PLD system was focused onto a rotating target of polycrystalline In_2O_3, which is approximately 6 cm from the MgO substrate surface. A substrate temperature of 500 °C and an O_2 partial pressure of approximately 20 mTorr were maintained during deposition. The laser system was allowed to run for 40,000 pulses at a rate of 10 Hz and an energy of 200 mJ/pulse. This resulted in an In_2O_3 film of thickness 1.5 μm. Further details on the PLD system are described elsewhere [54].

The coated substrate was then sectioned into smaller 4×2 mm samples. For reference, one of the samples, sample A, was reacted without an applied electric field. Another sample, sample B, was reacted under an applied electric field of 400 V. To apply the field during the reaction, sample B was placed between two Pt electrodes, the MgO substrate in contact with the anode and the In_2O_3 film in contact with the cathode. The electrodes were roughened to allow oxygen transport to the surface of the diffusion couple and then held in place by a slight mechanical pressure to ensure proper contact. Both samples were then placed inside a box furnace and heated at a rate of approximately 15 °C/min to the reaction temperature of 1350 °C. The reaction temperature was held for 12 min and then the samples were cooled to room temperature at a rate of about 20 °C/min.

Cross sections of the two samples were then prepared for analysis using the tripod-polishing technique, in which the samples were mounted and polished with successively finer grades of diamond-embedded

lapping films. The final polish was performed using 0.05 μm colloidal silica on a padded lapping film. Microstructural imaging was carried out using a field-emission SEM at 5 kV. The samples were then tilted in the microscope 70° and oriented such that the (001) pole of the MgO substrate, or the growth direction of the film, was parallel to the transverse direction (TD), and the interface direction was parallel to the reference direction (RD) (see Fig. 1). The SEM was operated at 20 kV for EBSD and XEDS analysis. The cross-section samples were coated with 2 nm of Pt to minimize charging. Elemental information was obtained using an X-ray energy-dispersive spectrometer (XEDS) system that is attached to the SEM.

An as-grown film of In_2O_3 was included in the analysis in order to determine the condition of the film prior to the reaction. The growth conditions for the as-0grown film were the same as those of the reaction couples except that the PLD system was operated for fewer pulses to deposit a thinner film of In_2O_3. A cross section of this sample was also prepared and analyzed by the above techniques.

Experimental results

The entire cross section of the as-grown In_2O_3 film was observed by SE imaging, and found to be of very uniform thickness. Figure 2a is an SE image of a small portion of the cross section, which is approximately 1.2 μm thick. The Pt markers can be seen as bright spots located at the interface of the film and substrate. EBSD analysis was performed on 46 μm of the film cross section. This area includes over 450 grains of the In_2O_3. Figure 2b was created using only a small section of the EBSD data. The figure is a combined IPF map and IQ map of the as-grown film, which illustrates the grain shape and growth direction of the In_2O_3 film. The IPF map, in this case, is a color representation of the crystallographic directions

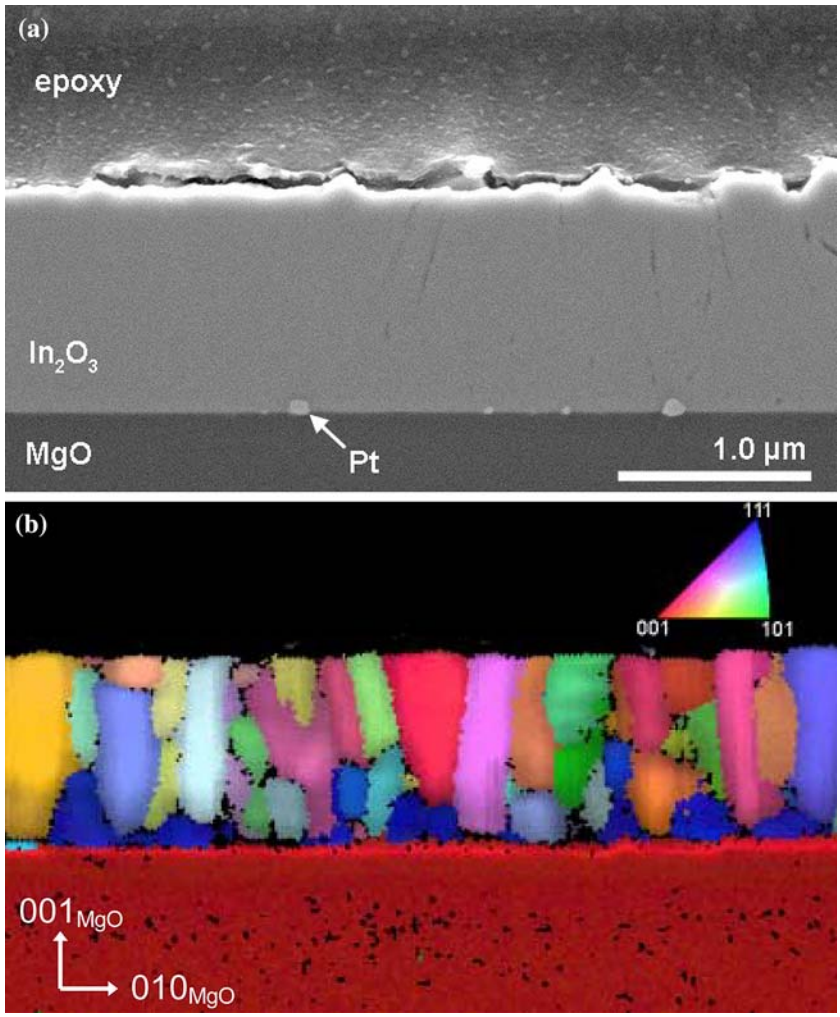

Fig. 2 (**a**) A secondary electron (SE) image and (**b**) an IPF map of the as-grown In_2O_3 film from different locations on the sample. The IPF map is superposed on an image quality map to give a slightly darker contrast to the grain boundaries. The crystal directions represented by the colors in (**b**), are parallel to the 001_{MgO} direction

that are parallel to the growth direction. The superimposed IQ map serves to give contrast to the grain boundaries and interface in order to emphasize the structure of the grains. The film is polycrystalline with columnar shaped grains, but it is difficult to detect a preferred growth orientation from this small image.

Figure 3 is an IPF map, which reveals a larger view of the film. As in Fig. 2b, it also represents the crystallographic directions parallel to the growth direction.

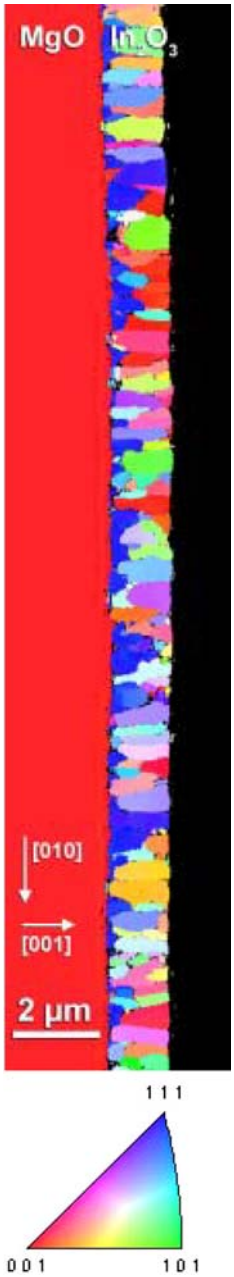

Fig. 3 An IPF map of a small area of the as-grown film cross section. The color of the grains indicates the crystallographic directions parallel to the growth direction

Now it can be seen that, near the interface, there is a large number of grains that have grown in such a way that the In_2O_3 (111) planes are parallel to the growth surface. Many of these grains, represented on the map in blue, do not extend to the top of the In_2O_3 layer. Figure 4 shows the texture pole figures that represent the orientations of all the grains only within the In_2O_3 as-grown film. The pole figures were calculated using one orientation per grain so that the grains are weighted equally irrespective of size. The pole figures are also oriented such that the pole marked ''TD'' is normal to the growth surface, or the MgO [001] direction. Therefore, the vertical line in the pole figure represents the location of the interface plane. The pole figures show that the predominant growth orientations of the grains in the film are first,

$$In_2O_3(111) \parallel MgO(001) \quad (1)$$

and second,

$$In_2O_3(001) \parallel MgO(001). \quad (2)$$

This is shown by the peaks located at the poles marked ''TD'' in both the 001 and 111 pole figures. They also show that there are several orientations tilted about these axes. In the 001 pole figure, there are two lines of peaks that are approximately 35° from the interface plane (indicated in Fig. 4). In the 111 pole figure there are two rows of peaks that are approximately 20° from the interface plane (also indicated in Fig. 4). These additional peaks indicate that for orientation (1), the in-plane orientations are:

$$In_2O_3[1\bar{1}0] \parallel MgO[110], \quad (1a)$$

which, combined with orientation (1), has four equivalent orientation variants. For orientation (2), the in-plane orientations can be seen on the pole figure as:

$$In_2O_3[100] \parallel MgO[100] \quad (2a)$$

and a very minor peak indicating the orientation:

$$In_2O_3[100] \parallel MgO[110]. \quad (2b)$$

The above orientation relationships, including all four variants of (1a), were plotted on pole figures to create the simulated pole figures in Fig. 5. From the EBSD data it was calculated that 15.3% of the cross-section area is within 5° of orientation (1), and 9.4% of the film is within 5° of orientation (2).

Sample A represents the reaction couple after annealing for 12 min at 1350 °C. A plan-view secondary-electron image of sample A, which shows the surface of the In_2O_3 film, is shown in Fig. 6. The grain size

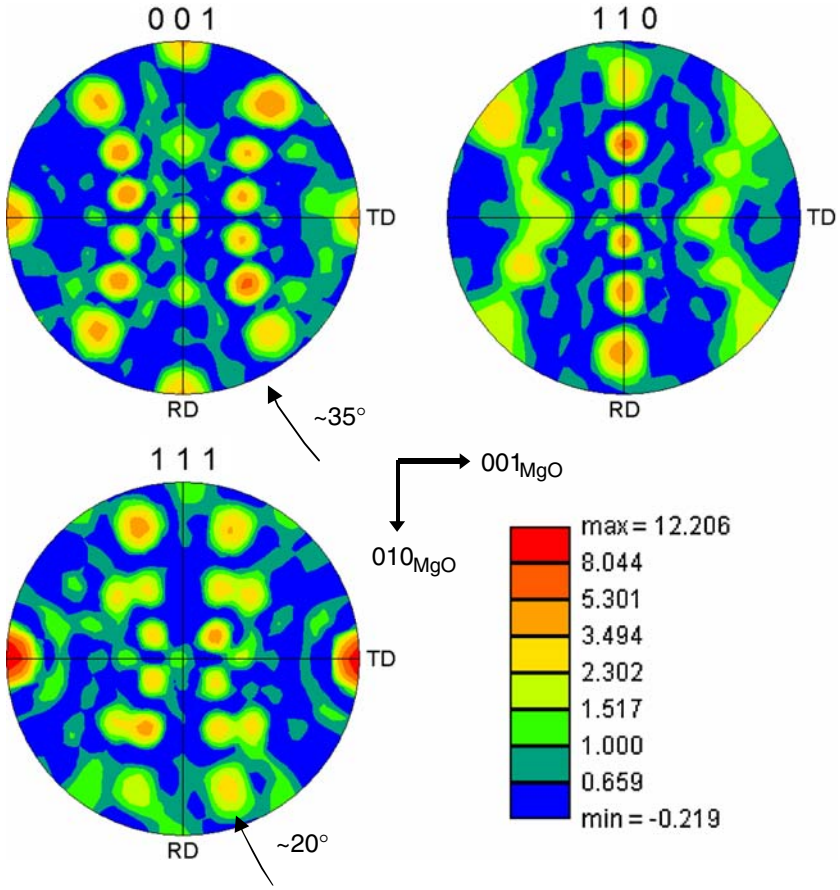

Fig. 4 Texture pole figures of the 001, 110 and 111 directions taken only from data points within the In_2O_3 film. The pole figures were calculated using one orientation per grain, and are oriented such that the pole marked "TD" is parallel to the MgO [001] direction and the vertical line represents the location of the interface plane

of the film is comparable with the film thickness, which is consistent with the formation of columnar grains as seen in the as-grown film. In order to confirm that the surface film was actually In_2O_3, EBSD was used in conjunction with EDS to perform phase identification of the film. Figure 7a shows a representative EDS spectrum from the annealed film. The spectrum confirms the presence of indium and oxygen, however, a quantitative analysis of the spectrum was not completed because the inherent error in performing this type of analyses on a highly tilted sample. (The sample was tilted to 70° in order to acquire the EBSD patterns.) The chemical composition was then used to search a database of materials and generate a list of candidate phases. These candidate phases were used to attempt to index the EBSD pattern, shown in Fig. 7b, that was acquired from the same grain as the EDS spectra. The crystallography of the phase was then determined by correctly indexing the pattern using the crystallographic information of the correct candidate phase. Figure 7c shows one of the EBSD patterns acquired from the annealed film with the indexing overlay of the correct candidate phase. It was determined that the film was the cubic, bixbyite phase of In_2O_3.

Figure 8 is an IPF map of the surface of the annealed film. It should be noted that the image in Fig. 8 is a tilt-corrected map of the surface. Therefore, the rounded appearance of the individual grains is exaggerated on the map image. The IPF map in this case represents the crystallographic directions of the material that are parallel to the surface normal of the plan-view sample. The black pixels are points from which the EBSD patterns were not of sufficient quality to be indexed. The EBSD data set used to create the map in Fig. 8, and for subsequent analysis, was comprised of over 1600 grains and over 85,000 orientation measurements from the annealed In_2O_3 film. It can be seen from the orientation map in Fig. 8 that there is a large number of In_2O_3 grains for which the $\langle 001 \rangle$ direction is closely parallel to the [001] direction of the MgO (these grains appear red in the IPF map). In fact, the texture plot in Fig. 9 shows that the occurrence of this orientation is 8–12 times greater than the random value. Of the grains with that alignment, approximately two-thirds of them also have the in-plane orientation (2a) while the other third have an orientation (2b). Figure 9 also shows that there is some rotation of orientation (2) toward the [110] directions of the MgO. This can be seen at the center of the texture plot as an

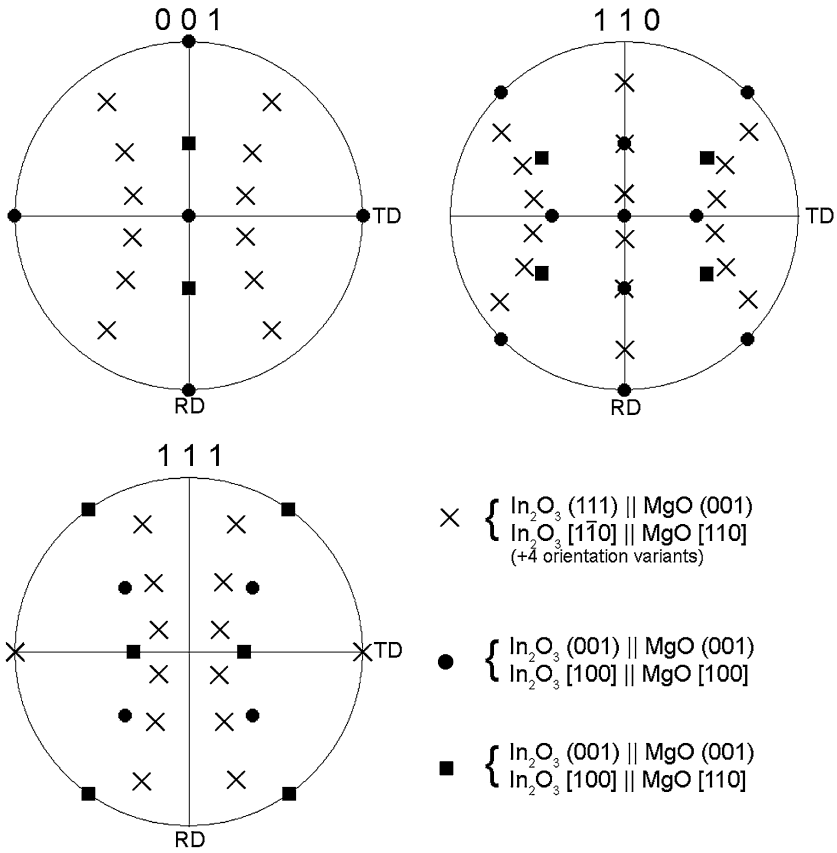

Fig. 5 Simulated texture pole figures of the 001, 110 and 111 directions using the three orientation relationships shown in the key above. The first relationship includes four orientation variants

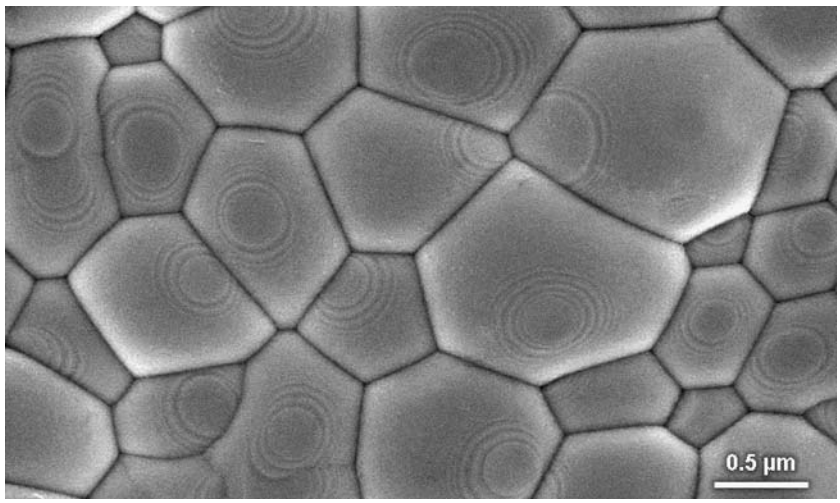

Fig. 6 Plan-view SE image from the In_2O_3 layer after annealing. The grain size (~1 μm) is comparable to the thickness of the layer. The circular features on the grains are a result of faceting at the surface due to the anneal treatment. The region inside the center circle is flat and likely corresponds to the (001) plane of the In_2O_3

"×" shape of the texture-contour lines or the texture-contour lines forming "corners" that point toward the [110]-MgO directions.

The results of the reaction that takes place in sample A are illustrated in Fig. 10, which is an SE image of a cross section of the reaction couple. In the absence of the applied field, the layers have only partially reacted. The spinel reaction product (with an intermediate SE contrast) is seen to form at the interface between MgO (very dark gray) and In_2O_3 (light gray). From the image it is apparent that reaction rate is not equivalent at all points along the interface, and the Pt markers (bright spots) are found to be located within the spinel layer [8, 26].

EBSD analysis was carried out on a cross section of sample A to confirm the phase of the reaction layer and to obtain orientation information for the grains in the reaction layer with respect to the MgO substrate

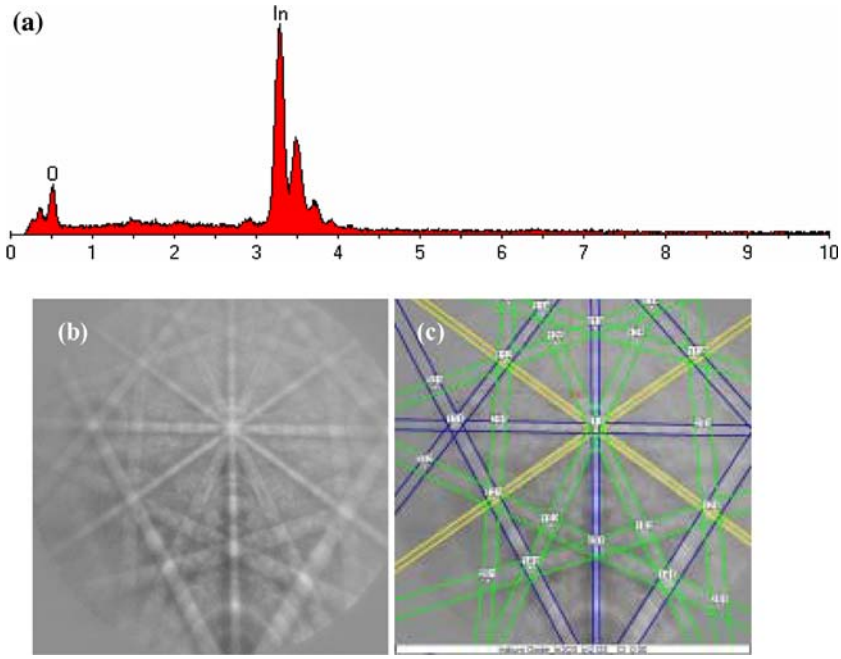

Fig. 7 Representative data used to identify the as-grown film as the cubic form of In_2O_3. Images include an EDS spectrum (**a**) and an EBSD pattern without (**b**) and with (**c**) the indexing overlay from the correct candidate phase

and the In_2O_3 layer. An XEDS spectrum was acquired from the reaction layer and is shown in Fig. 11a. The spectrum reveals the presence of a magnesium peak in addition to the indium and oxygen peaks. EBSD patterns acquired from the reaction layer suggest a cubic crystal structure and the pattern indexing indicated the spinel structure of $MgIn_2O_4$. An example of one of the patterns acquired from the reaction layer and used for indexing and identification is shown in Fig. 11b, c.

As part of the EBSD analysis, sample A was scanned in 50 nm steps over an area that included a 135 μm length of the reaction layer, which included over 700 grains from the In_2O_3 layer and over 80 grains from the reaction layer. The data collected at each point included the EBSD pattern and XEDS counts for the energy levels associated with Mg, Li and O. Figure 12 shows a 24 μm section of the 135 μm length of scanned area. Figure 12 is an IQ map, an IPF map and a phase map. The IQ map reveals many of the grain boundaries—which can be seen as darker lines outlining the grains—and other points of low pattern quality. The IPF map again shows the crystallographic directions that are parallel to the surface normal of the cross-section sample. The phase map was created using both X-ray counts and EBSD pattern indexing to differentiate the three phases.

From the EBSD data, several characteristics of the grains of the reaction couple were recognized. The IPF map in Fig. 12 indicates that there are several grains in the reaction layer that are aligned with the MgO [001] direction. In fact, it was found that many grains possess a cube-to-cube orientation with the MgO substrate. However, it is clear that the film is polycrystalline. Also, the predominant grain shape of the $MgIn_2O_4$ reaction layer is such that the cross-section length of the grains (dimension parallel to the interface) is much larger than the thickness of the grains. However, it was found that this cross-section length varied widely, from 0.5 μm up to tens of microns. This is distinctly different from the In_2O_4 overlayer, in which the grains are more of a columnar shape. The thickness of the reaction film was found to vary only slightly from grain to grain, when measured at the grain centers or far from the

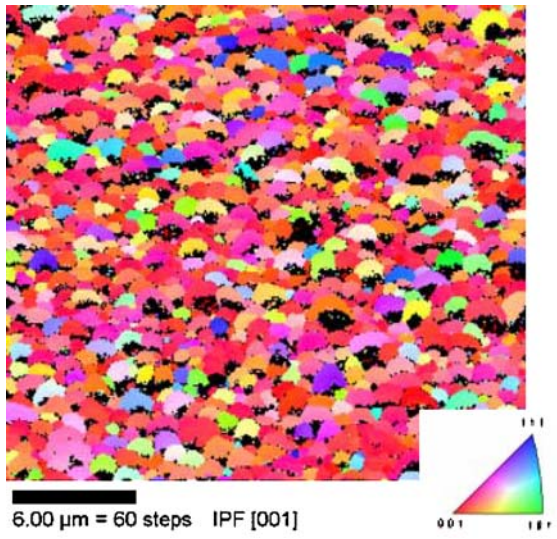

Fig. 8 An inverse pole figure (IPF) map of the surface of the as-grown In_2O_3 film. The key for the IPF map is shown on the right

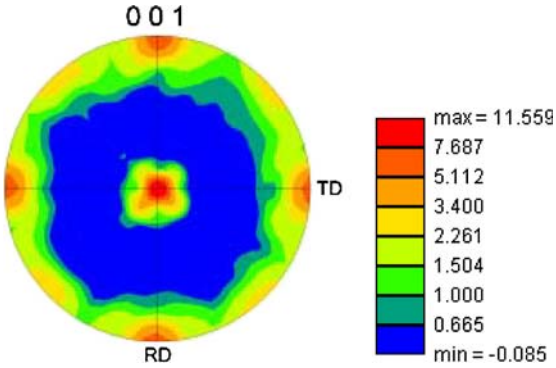

Fig. 9 A texture pole figure calculated from the same dataset used to create the IPF map in Fig. 3. The figure displays the [001] texture of the film with respect to the substrate. The key on the left indicates, by color, the multiple times random occurrence of the <001>-type crystallographic direction. TD and RD represent the transverse direction and the reference direction of the sample which are aligned with the *y*-axis and the *x*-axis of the MgO substrate respectively

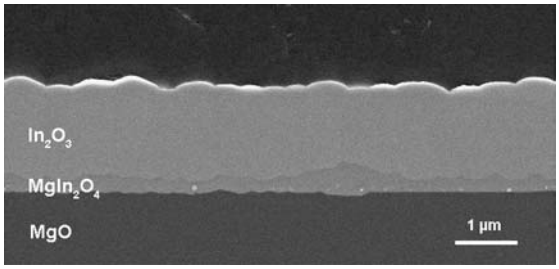

Fig. 10 SE image from sample A. Only partial reaction to $MgIn_2O_4$ spinel has taken place. The bright spots located within the reaction layer are the Pt markers

grain boundaries. Greater variations, however, were found near the grain boundaries. The average reaction layer thickness excluding the regions near the grain boundaries was calculated from the EBSD data to be approximately 0.32 μm.

The greater variations in the reaction layer thickness indicate regions of the reaction layer that have grown much faster than adjacent regions. Closer examination of the three maps in Fig. 12 reveals that the faster growth is often associated with the grain boundaries in the $MgIn_2O_4$ layer (indicated by arrows on the IQ map in Fig. 12). Grain-boundary analysis was performed using the EBSD data, which indicated that, along the 135 μm length of the cross section that was analyzed, all of the $MgIn_2O_4$ grain boundaries associated with a faster reaction rate, had large-angle misorientations. Furthermore, there were very few large-angle grain boundaries that were not associated with a faster reaction rate. The small-angle grain boundaries that were present in the reaction layer were not associated with a faster reaction rate. An example of the variations in reaction layer growth associated with different grain boundary types is shown in Fig. 13, which is a schematic of the grains and grain boundaries of a representative portion of the sample A cross section. The reaction layer grain boundaries in the schematic are labeled with the misorientation angle of the adjacent grains. The misorientations are further illustrated by schematics of the cubic unit cell for each grain in the reaction layer. The regions that immediately surround the boundaries with large misorientations have reacted

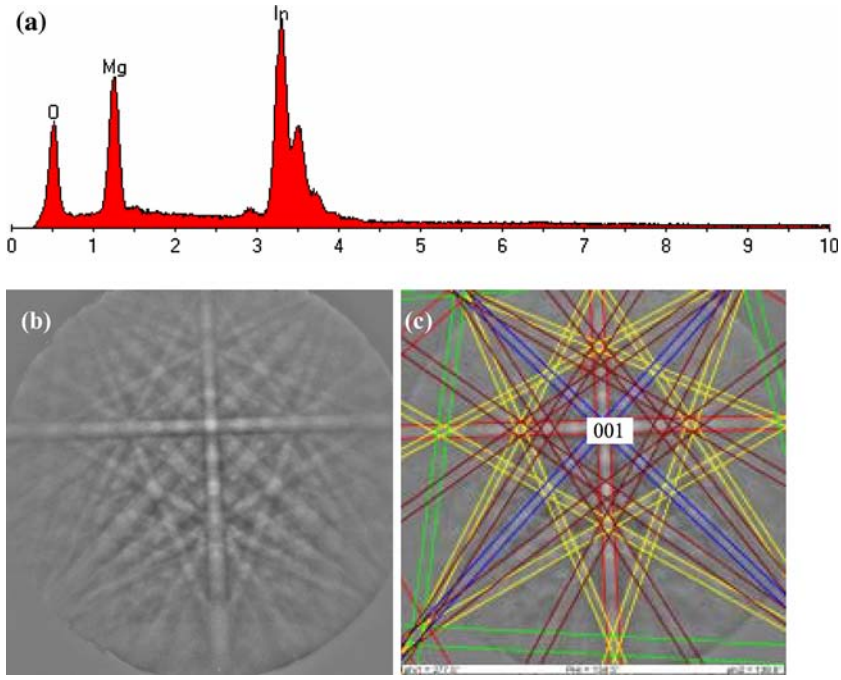

Fig. 11 Representative data used to identify the reaction product layer as the cubic/spinel form of $MgIn_2O_4$. Images include an EDS spectrum (**a**) and an EBSD pattern without (**b**) and with (**c**) the indexing overlay from the correct candidate phase

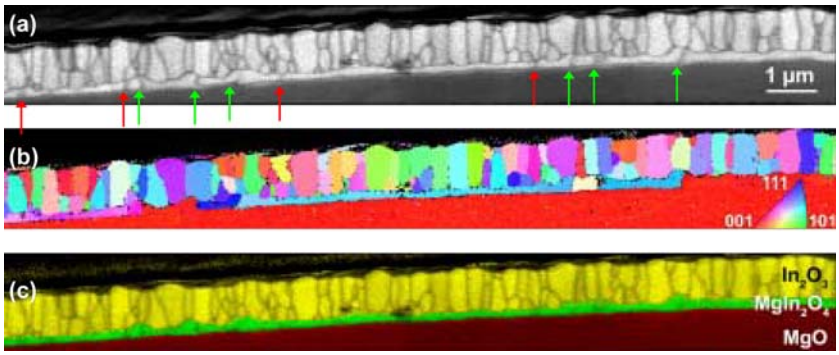

Fig. 12 An image quality map (**a**), an inverse pole figure map (**b**), and a phase map (**c**) of a section of the scanned area from sample A. The phase map is overlaying an IQ map to give the grain boundaries contrast. The arrows in the IQ map indicate the location of grain boundaries in the $MgIn_2O_4$. The red arrows point to small-angle boundaries (<12°) and the green arrows point to the large-angle boundaries (>12°)

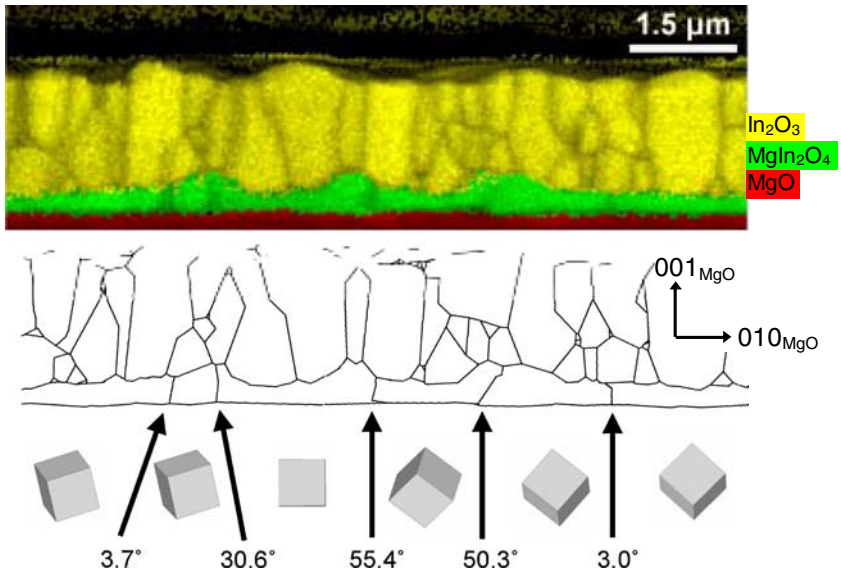

Fig. 13 (Top) A phase map superposed on an IQ map, which shows a portion of the sample A cross section. (center) A schematic of the grains and grain boundaries corresponding to the above map. (bottom) The grain boundaries in the reaction layer schematic are labeled with the angle of misorientation of the adjacent grains. The orientations of the reaction layer grains are illustrated by schematics of the cubic unit cell shown directly below the grains they represent

at a much faster rate than the regions surrounding the boundaries with small misorientations.

Figure 14 is an SE image from sample B, which was annealed at 1350 °C for 12 min under an applied field of 400 V. From the image it can be seen that there is now only one layer of material that is surrounded on both sides by the MgO. It was confirmed by EDS and EBSD that the layer with intermediate contrast was the spinel phase of $MgIn_2O_4$, and that the surrounding (darker) material was MgO. Therefore, under the above reaction conditions, all of the In_2O_3 had been consumed to create the spinel layer, and a continuous layer of MgO was formed above the spinel, away from the MgO substrate. Furthermore, many of the Pt markers are now located in the MgO substrate. The reaction layer of sample B has a non-uniform thickness, and the interface between the reaction layer and the original MgO substrate is very irregular. In some regions of the substrate/reaction layer interface there appear ''spikes'' of the substrate material pointing into the reaction layer. It was found that some of these features extended completely into the overgrown MgO to create a discontinuity in the reaction layer.

EBSD analysis was performed on sample B by scanning a cross section of the sample in 50 nm steps. Figure 15 shows a small portion of the scanned cross section as an IQ map, an IPF map and a phase map. From the phase map it can be seen that the grains within the $MgIn_2O_4$ spinel layer are also non-uniform in size. A comparison of the IPF and IQ maps shows that the reaction layer is composed of grains and grain boundaries that are irregular and dissimilar from the grains of either the original In_2O_3 layer or the reaction product layer found in sample A. The layer of

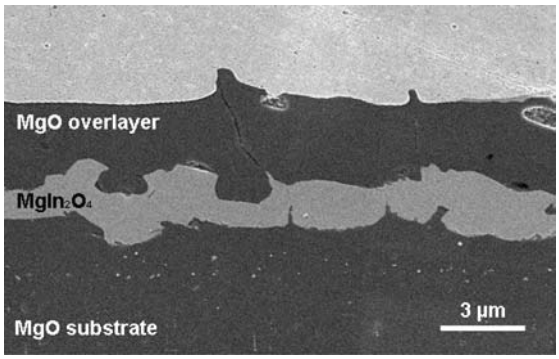

Fig. 14 SE image from sample B indicating that the In_2O_3 layer has fully reacted to form the $MgIn_2O_4$ spinel. An overgrown layer of MgO is seen on top of the spinel layer. The top portion (bright) is from the Pt electrode

overgrown MgO appears to be the same approximate thickness as the reaction layer, however, on average the grains of MgO appear larger than those of the reaction layer. The IPF map also shows that there are large regions of the reaction layer, as well as grains in the MgO overlayer, that are closely oriented with the MgO substrate. However, it was found that the oriented regions of the reaction layer, contain numerous small-angle grain boundaries. An example of such an area is magnified in Fig. 16a where a color map is superposed on an IQ map. The color map shows the degree of misorientation (0–15°) from perfect alignment with the MgO substrate. The underlying IQ map reveals all of the grain boundaries as darker lines in the map. There are several larger grains in the reaction layer, which are more than 15° from perfect alignment with the MgO substrate. It can also be seen that these larger grains do not contain small-angle grain boundaries. The regions with more small-angle grain boundaries are much closer to being aligned with the MgO substrate.

Discussion

The In_2O_3 films grown for this experiment were found to be polycrystalline with a columnar grain structure. The EBSD data shown in Figs. 3 and 4 indicate that the preferred orientations of the films may change across the thickness of the layer. This was confirmed by

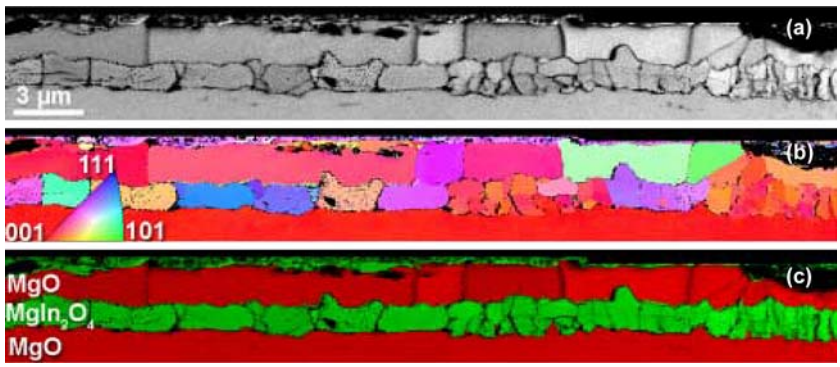

Fig. 15 An image quality map (**a**), an inverse pole figure map (**b**), and a phase map of a section of the scanned area from sample B. The MgO substrate is on the far right of the images. The region on the far left is the platinum cathode

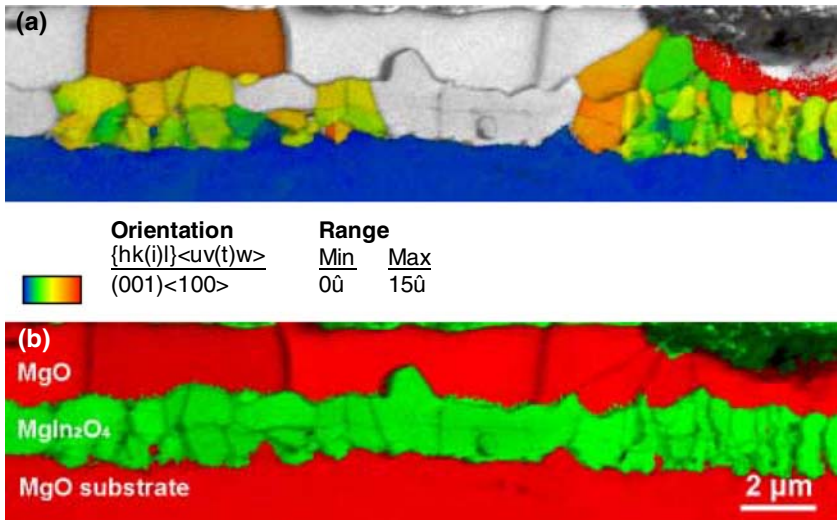

Fig. 16 (**a**) A crystal orientation map superposed on an IQ map. The crystal orientation map shows by color the degree of misorientation from perfect alignment with the MgO substrate. The underlying IQ map, of course, reveals the grain boundaries as darker lines in the map. The key is shown below the map. (**b**) A phase map, superposed on an IQ map, is shown for reference

recalculating the texture pole figures in Fig. 4 for the top and the bottom 0.6 μm of the film separately. Figure 17 shows separate cross sections of the (111) and (001) texture pole figures for both the bottom and top halves of the In_2O_3 film. In this figure, the growth direction is centered at 0° and the cross section only goes out to 45°, or out parallel to the MgO [101] and [$\bar{1}$01] directions. The figures show that for the bottom 0.6 μm of film (that closest to the interface), the fraction of material that is within 2° of orientation (1) is 26.4%; for the top 0.6 μm, the amount drops to approximately 2%. The fraction of material within 2° of orientation (2) in the bottom half of the film was found to be 3.4%; whereas in the top half it increases to 6%. Under the described experimental conditions, therefore, it appears that the early stages of the In_2O_3 film deposition predominantly occurs with the (111) planes parallel to the surface of the substrate and the growth proceeding in the [111] direction of the film. At a later stage in the growth process, however, the predominant growth direction becomes the [001] direction of the film. This interpretation is also strongly supported by the texture pole figure shown in Fig. 9, which was calculated from data acquired from the top surface of the annealed film. This figure shows that, at the surface, the predominant orientation is that of (2). The misorientation between the two predominant growth directions can be explained by a tilt of 54.7° about a common [110] axis that is within the interface plane.

Previous studies have shown the existence of both growth orientations. Highly oriented, cube-on-cube growth of very thin (~350 nm) In_2O_3 films has been reported for growth by PLD at 400–450 °C on (001) MgO substrates [47]. Sieber et al. have reported that with increasing substrate temperature the amount of film possessing the (2 – 2a) orientation decreases and the amount with the (1 – 1a) orientation increases. In that study, highly oriented films were grown by electron-beam evaporation to thicknesses of between 120 nm and 150 nm, and substrate temperatures from 600 °C to 850 °C. Sieber et al. also reported that the growth resulted in columnar-type grain growth [44]. However, these studies did not find a change in the preferred orientation across the thickness of the film.

The differences between the results of the present work and those of previous workers are likely caused by several differences between the experimental conditions. In the present work, the films are much thicker (>1.0 μm). The substrates have been cleaved and annealed in preparation for growth, instead of acid etching/cleaning. Another significant difference is the deposition and dewetting of the Pt film prior to the In_2O_3 film growth, which was carried out for the purpose of creating a marker for the initial position of the substrate-film interface. The use of Pt markers in solid-state reactions has been previously studied, and it has been shown that the dewet Pt islands on the surface of the MgO may affect the growth and reaction of the film [8].

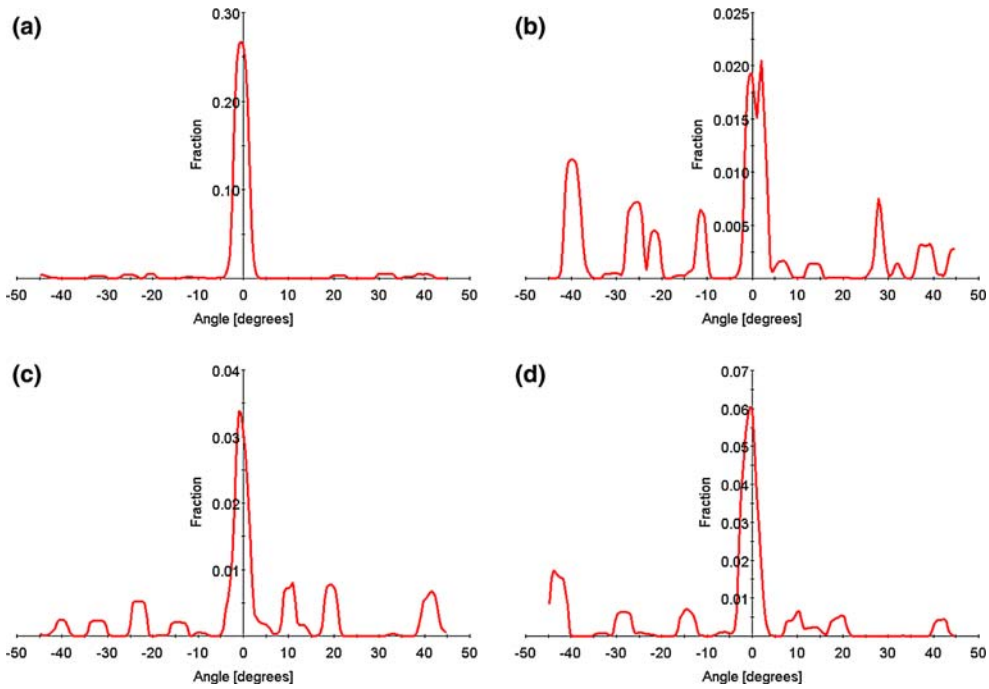

Fig. 17 Charts representing cross sections of the (111) texture pole figures for the bottom (**a**) and top (**b**) 0.6 μm of the In_2O_3 film, and charts representing cross sections of the (001) texture pole figures for the bottom (**c**) and top (**d**) 0.6 μm of the In_2O_3 film. In the above charts, the growth direction is centered at 0° and the cross section only goes out to 45°, or out parallel to the MgO [101] and [$\bar{1}$01] directions. The charts were created using every data point instead of one point per grain so that they represent an area fraction of the film cross section, not a grain fraction

In sample A the Pt markers are located within the reaction layer. In the absence of an applied electric field, the spinel forming reaction is known to be controlled by the counter-diffusion of cations and follow a parabolic growth rate [18, 19]. Therefore, the Pt marker positions in sample A are qualitatively in agreement with the counter-diffusion of cations since, in that case, the reaction would be taking place on both sides of the marker or both ''sides'' of the original interface [8].

The counter-diffusion of cations does not, however, adequately explain why there are differences in the reaction rate along the interface. The EBSD data have shown that the reaction layer is polycrystalline (see Fig. 12), and that the greatest inconsistencies in reaction rate occurred at or near large-angle grain boundaries. In these regions, it is expected that the reaction rate would be affected by the occurrence of grain-boundary diffusion and the excess volume at the grain boundary [17]. In addition to this, however, there were smaller differences in the reaction layer thickness from grain to grain when measured at the grain centers or far from the large-angle grain boundaries. This observation indicates that the reaction rate is also dependent on the orientation of the reaction layer or rather the misorientation between the reaction layer and the substrate or the reaction layer and the In_2O_3 film.

The kinetic processes—which occur in the materials during reactions—can be either interface-controlled or diffusion-controlled. The interface-controlled regime is typically associated with the early stages of the reaction and exhibited by a linear reaction rate. The diffusion-controlled reaction regime, which occurs when the thickness of the layer becomes great enough to control the diffusion process, is associated with a parabolic reaction rate [18, 19]. The two large differences in reaction rates exhibited by sample A can also be associated with these two kinetic regimes.

The smaller reaction-rate variations, which occur from grain to grain, are observed far from the grain boundaries. It is most likely that these differences are caused by a difference in the orientations of the grains themselves, or a difference in the misorientations between the reaction layer grains and the MgO substrate or between the reaction layer grains and those of the In_2O_3 film. It has been shown that the nucleation of solid-state reaction product layers may occur at triple junctions, where a grain boundary in one of the reactants meets the reaction interface [17]. However, once the reaction product layer has nucleated, the formation of this layer along the interface may occur rapidly as there is very little, or no material at all, for the ions to diffuse across. In this state, it is the structure of the interface that has the greater affect on the reaction rate [11]. The misorientation at the interface, in large part, defines the structure of the interface especially on the substrate side of the reaction layer, since the original interface plane of the substrate is fixed. Therefore, during the early stages of the reaction the inconsistencies in reaction rate from grain to grain would be caused by the structural differences along the interface, which are themselves caused by the different misorientations.

As the reaction progresses, the thickness of the reaction layer becomes such that the reaction rate becomes limited by diffusion. The rate is no longer limited by the structure of the interface, but by differences in ion diffusion rates. If adjacent nucleation islands have a large misorientation, then the coalescence of these islands would create a large-angle grain boundary, as was found in sample A. A large-angle grain boundary typically has a more open structure than that of a small-angle grain boundary or the bulk. This would allow for much faster diffusion than that occurring through the bulk. Therefore, the difference in reaction rate in the diffusion-controlled regime is caused by a difference in diffusion rates of the ions through the grain boundaries versus through the bulk material.

Sample B illustrates that the application of the electric field resulted in the complete consumption of the In_2O_3 layer (i.e., complete reaction). Then further transport of Mg ions across the spinel phase and formation of MgO on the opposite side of the reaction-product layer. This is explained by the fact that in the presence of an applied field, in addition to the counter-diffusion of the cations, there is a superimposed flux of cations towards the negative electrode [9, 25], which leads to a shift of the reaction layer toward the anode. In addition, many of the Pt markers are now located in the MgO substrate.

One of the interesting features found in sample B that can be seen in the image in Fig. 14, is the appearance of MgO ''spikes'' that penetrate the reaction layer. Although these features may appear as spikes, their complete physical dimensions cannot be fully characterized by a cross section. In fact, it was found that some of the spikes continued into the overgrown reaction layer, becoming discontinuities in the reaction layer. The EBSD data indicated that the spikes were located at the grain boundaries that are found within the reaction layer, so that the spikes appear partially to separate some of the grains of the reaction layer. Unfortunately, the amount of EBSD data collected was insufficient to determine if there was a correlation between the types of grain boundaries in the reaction layer and the presence of a spike or

reaction layer discontinuity. However, the observation of grains in the overgrown MgO, which maintain the orientation of the substrate, supports the possibility that discontinuities in the reaction layer act to nucleate the MgO overlayer.

Conclusions

The reaction between MgO and In_2O_3 thin films to form the $MgIn_2O_4$ spinel has been characterized by EBSD. The as-grown film was grown by PLD, and the phase was identified by EBSD and EDS to be In_2O_3 with the cubic, bixbyite structure. The film was found to be composed of columnar grains of In_2O_3. It was shown that the preferred growth directions of the as-grown films were found to change across the thickness. The bottom 0.6 μm of the film, that closest to the interface, was found to have a preferred growth direction represented by orientation (1). The top 0.6 μm of the film was found to have a preferred growth direction represented by orientation (2). Therefore, the early stages of the In_2O_3 film deposition predominantly occurs with the growth proceeding in the [111] direction of the film. At a late stage in the growth process the predominant growth direction becomes the [001] direction of the film.

Sample A was found to be partially reacted. The reaction layer was identified as the spinel phase of $MgIn_2O_4$. It was shown that the reaction layer is polycrystalline and that the thickness of the reaction layer and therefore the reaction rate is non-uniform. The greatest inconsistencies in reaction rate occurred at or near large-angle grain boundaries, and are associated with the diffusion-controlled reaction regime. The smaller differences in the reaction layer thickness occurred from grain to grain, measured at the grain centers or far from the grain boundaries. These smaller differences stem from the differences in misorientation between the reaction layer and the substrate or the reaction layer and the In_2O_3 film. Further study, using a broader range of reaction times and different substrate orientations, is needed to confirm and identify the orientation dependence of the reaction rate in the interface-controlled reaction regime.

It was also confirmed by sample B that the application of the electric field resulted in a complete reaction, and then further transport of Mg ions across the reaction layer. The formation of a layer of MgO on the opposite side of the reaction layer is explained by the fact that there is an additional flux of cations towards the negative electrode. The new MgO layer was found to be polycrystalline with larger average grain size than the reaction layer. Several grains were found exhibiting the same orientation as that of the MgO substrate, indicating that the nucleation of the overlayer may occur at discontinuities in the reaction layer.

Finally, it has been demonstrated that the application of EBSD to study the development of texture in solid-state reactions compliments more detailed analysis in the TEM and indeed should always precede any TEM analysis. The EBSD technique provides statistical data on the type of interface selected for such detailed studies.

Acknowledgements The authors would like to thank Prof. N. Ravishankar, Dr. Carsten Korte and Dr. Matt Johnson for extensive discussions relating to this work. The experimental part of this study was carried out at the University of Minnesota and at the laboratories of TSL in Utah. This research has been supported by the 3M Heltzer Endowed Chair and the US Department of Energy under Grant Numbers DE-FG02-92 ER45465-A004 and DE-FG02-01ER45883.

References

1. Worrell WL (1988) Solid State Ionics 28–30:1215
2. Julien C (2003) Solid State Ionics 157:57
3. Mackenzie KJD, Ryan MJ (1981) J Mater Sci 16:579
4. Brown IWM, Mackenzie KJD (1982) J Mater Sci 17:3663
5. Schmalzried H, Smolin S (1998) Ber Bunsen-Gesell-Phys Chem, Chem Phys 102:1740
6. Johnson MT, Schmalzried H, Carter CB (1997) Solid State Ionics 101–103:1327
7. Johnson MT, Gilliss SR, Carter CB (1998) Microsc Microanal 4:158
8. Johnson MT, Carter CB (1999) Phil Mag Lett 79:609
9. Korte C, Ravishankar N, Carter CB, Schmalzried H (2002) Solid State Ionics 148:111
10. Korte C, Farrer JK, Ravishankar N, Schmalzried H, Michael JR, Carter CB (2000) Mater Res Soc Symp Proc 586:151, MRS, Warendale, PA, Boston, MA
11. Schmalzried H (1995) Chemical kinetics of solids, VCH
12. Schmalzried H (1981) Solid state reactions, 2nd edn. Verlag Chemie
13. Pfeiffer T, Schmalzried H (1989) Z Phys Chem Neue Folge 161:1
14. Wagner C (1936) Z Phys Chem B34:309
15. Simpson YK, Carter CB (1987) Mater Res Soc Symp Proc 94:45
16. Becker KD (1994) In: d'Heurle FM, Gas P, Martin M, Philibert J (eds) Reactive formation of phases at interfaces and diffusive processes, vol 155–156. Trans Tech Publications
17. Kotula PG, Johnson MT, Carter CB (1998) Z Phys Chem 206:73
18. Wagner C (1938) Z Anorg Allgem Chem NF148:21
19. Schmalzried H (1962) Z Phys Chem Neue Folge 33:111
20. Simpson YK (1989) Grain Boundaries, Phase Boundaries and Reactions in Ceramic Oxides. Ph.D. Thesis, Cornell University
21. Kotula PG, Carter CB (1998) J Am Ceram Soc 81:2869
22. Kotula PG, Carter CB (1995) Proceedings of the 53rd Annual Meeting of MSA, 338

23. Thirsk HR, Whitmore EJ (1940) Trans Faraday Soc 36:565
24. Kotula PG, Carter CB (1995) Scripta Metall 32:863
25. Johnson MT, Carter CB (1997) Solid State Ionics 101–103:1327
26. Johnson MT, Carter CB (1998) Microsc Microanal 4(2):141
27. Senz S, Blum W, Hesse D (2001) Phil Mag A 81:109
28. Jing S-Y, Lin L-B, Huang N-K, Zhang J, Lu Y (2000) J Mater Sci Lett 19:225
29. Huang M-R, Lin C-W, Lu H-Y (2001) Appl Surf Sci 177:103
30. Susnitzky DW, Carter CB (1991) J Mater Res 6:1958
31. Kotula PG, Carter CB (1998) J Am Ceram Soc 81:2877
32. Johnson MT, Heffelfinger JR, Kotula PG, Carter CB (1997) J Microsc 185:225
33. Johnson MT, Kotula PG, Carter CB (1997) In: Pond CEA (ed) Boundaries and Interfaces in Materials: David A. Smith Symposium. Proceedings of the Memorial Symposium. TMS, Indiannapolis, p 141
34. Werner P, Sieber H, Hillebrand R, Hesse D (1997) Mater Res Soc Symp Proc 466:191, MRS, Warrendale, PA, USA, Boston, MA
35. Hesse D (1997) Solid State Ionics 95:1
36. Goehner RP, Michael JR (1996) J Res Nat Inst Standard Tech 101:301
37. Schwarzer RA (1996) Ultramicroscopy 67:19
38. Randle V (1992) Microtexture determination. The Institute of Materials
39. Adams BL (1997) Ultramicroscopy 67:11
40. Farrer JK, Carter CB, Ravishankar N (2006) J Mater Sci 41: 661
41. Farrer JK, Carter CB (2006) J Mater Sci 41: 779
42. Pijolat C, Riviere B, Kamionka M, Viricelle JP, Breuil P (2003) J Mater Sci 38:4333
43. Chopra KL (1983) Thin Solid Films 102:1
44. Sieber H, Senz S, Hesse D (1997) Thin Solid Films 303:216
45. Kamei M, Shigesato Y, Takaki S (1995) Thin Solid Films 259:38
46. Taga N, Odaka H, Shigesato Y, Yasui I, Kamei M, Haynes TE (1996) J Appl Phys 80:978
47. Tarsa EJ, English JH, Speck JS (1993) Appl Phys Lett 62:2332
48. Farrer JK, Michael JR, Carter CB (200) In: Schwartz AJ, Kumar M, Adams BL (eds) Electron backscatter diffraction in materials science. Kluwer Academic/Plenum Publishers, p 299
49. Michael JR (2000) In: Schwartz AJ, Kumar M, Adams BL (eds) Electron backscatter diffraction in materials science. Kluwer Academic/Plenum Publishers, p 75
50. Krieger-Lassen NC, Conradsen K, Juul Jensen D (1992) Scanning Microsc 6:115
51. Wright SI (2000) In: Schwartz AJ, Kumar M, Adams BL (eds) Electron backscatter diffraction in materials science. Kluwer Academic/Plenum Publishers, p 51
52. Bunge H-J (1982) Texture analysis in materials science: mathematical methods. Butterworths
53. Nowell MM, Wright SI (2004) J Microsc 213:296
54. Kotula PG, Carter CB (1993) In: Proceedings of the 2nd International Conference on Laser Ablation, Knoxville, TN, p 231